Astronomy & Astrophysics

The CARMENES search for exoplanets around M dwarfs

Convective shift and starspot constraints from chromatic radial velocities

D. Baroch[1,2], J. C. Morales[1,2], I. Ribas[1,2], E. Herrero[1,2], A. Rosich[1,2], M. Perger[1,2], G. Anglada-Escudé[1,2],
A. Reiners[3], J. A. Caballero[4], A. Quirrenbach[5], P. J. Amado[6], S. V. Jeffers[3], C. Cifuentes[4], V. M. Passegger[7,8],
A. Schweitzer[7], M. Lafarga[1,2], F. F. Bauer[6], V. J. S. Béjar[9,10], J. Colomé[1,2], M. Cortés-Contreras[4,11], S. Dreizler[3],
D. Galadí-Enríquez[12], A. P. Hatzes[13], Th. Henning[14], A. Kaminski[5], M. Kürster[14], D. Montes[15],
C. Rodríguez-López[6], and M. Zechmeister[3]

(Affiliations can be found after the references)

ABSTRACT

Context. Variability caused by stellar activity represents a challenge to the discovery and characterization of terrestrial exoplanets and complicates the interpretation of atmospheric planetary signals.

Aims. We aim to use a detailed modeling tool to reproduce the effect of active regions on radial velocity measurements, which aids the identification of the key parameters that have an impact on the induced variability.

Methods. We analyzed the effect of stellar activity on radial velocities as a function of wavelength by simulating the impact of the properties of spots, shifts induced by convective motions, and rotation. We focused our modeling effort on the active star YZ CMi (GJ 285), which was photometrically and spectroscopically monitored with CARMENES and the Telescopi *Joan Oró*.

Results. We demonstrate that radial velocity curves at different wavelengths yield determinations of key properties of active regions, including spot-filling factor, temperature contrast, and location, thus solving the degeneracy between them. Most notably, our model is also sensitive to convective motions. Results indicate a reduced convective shift for M dwarfs when compared to solar-type stars (in agreement with theoretical extrapolations) and points to a small global convective redshift instead of blueshift.

Conclusions. Using a novel approach based on simultaneous chromatic radial velocities and light curves, we can set strong constraints on stellar activity, including an elusive parameter such as the net convective motion effect.

Key words. convection – stars: late-type – starspots – stars: activity – techniques: radial velocities

1. Introduction

Late-type dwarf stars are a strong focus of attention in the search for Earth-like planets using radial velocities (RVs), because the amplitude of their signals is larger than for solar-type stars (e.g., Marcy & Butler 1998; Bonfils et al. 2013; Perger et al. 2017). However, with state-of-the-art instruments reaching $\sim 1\,\text{m\,s}^{-1}$ or even better uncertainties, it is not instrumental precision but astrophysical jitter that effectively limits the detection of exoplanets. This is particularly the case of some M-dwarf stars, because their intrinsic high level of magnetic activity causes the appearance of photospheric features such as stellar spots producing signals associated with the rotation period, which can hamper exoplanet detection efforts (Benedict et al. 1993). Several works discussing controversial exoplanet detections due to the stellar intrinsic jitter or spurious signals in RV curves caused by data treatment have been published (see, e.g., Robertson et al. 2014, 2015; Rajpaul et al. 2015). This reflects the difficulty of disentangling exoplanet signals from stellar jitter, even with the aid of stellar activity indices derived from spectroscopic data. However, it is also obvious that precise modeling of spot properties can help to disentangle and correct for stellar activity effects, thus enabling the detection of exoplanet signals that would otherwise be hidden within the stellar RV jitter.

A number of studies have shown that RV variability caused by stellar spots is wavelength dependent, because the flux contrast of cold spots and hot faculae is smaller toward the infrared (Desort et al. 2007; Reiners et al. 2010). Thus, in principle, measurements obtained at different spectral bands can be used to correct for intrinsic stellar RV jitter. However, the picture may be much more complicated because the effects of limb darkening, convection, and magnetic field, for instance, can cause both amplitude and phase differences between radial velocities derived from spectra at different wavelengths. On the other hand, these differential wavelength-dependent effects can be used to constrain the properties of stellar active regions.

The influence of stellar heterogeneities on RVs has been thoroughly studied in the past years by modeling the stars with surface elements at different effective temperatures representing the immaculate photosphere, spots, and faculae (see, e.g., Saar & Donahue 1997; Hatzes 2002; Lanza et al. 2007; Boisse et al. 2012). Photometric and RV variability due to stellar spots are then computed by disk-integrating the spectra corresponding to each surface element at different rotation phases. This approach only takes into account the effect of the flux dependence with effective temperature.

It is well known that the presence of magnetic fields also changes the properties of the convective layer of dwarf stars (Title et al. 1987; Hanslmeier et al. 1991). Convective cells cause significant effects on RVs, as motions produce net shifts and distortions on spectral lines (Dravins 1999; Livingston et al. 1999). For example, Gray (2009) and Meunier et al. (2017) showed that RVs derived from different spectral lines depend on the depth of the line, which also affects the shape and absolute shift of the

cross-correlation function bisectors. This makes the estimation of stellar convective motions strongly dependent on the spectral lines employed and on the temperature distribution of surface elements at the time of observation. This is true even for the Sun, for which measures of convective (blue)shift range from $200\,\text{m s}^{-1}$ to $500\,\text{m s}^{-1}$ (Meunier et al. 2010; Lanza et al. 2010). Meunier et al. (2017) used the differential Doppler displacement between the spectral lines and their dependence on the line depth to compute the convective shift for a sample of G0 to K2 main-sequence stars, and found that the absolute value of the convective shift decreases toward cooler stars. Hydrodynamic numerical simulations performed by Allende Prieto et al. (2013) showed a similar dependence of the convective blueshift on spectral type. However, there appear to be no direct measurements of the convective shift for M dwarfs, and it is not yet certain if the decreasing trend of the convective shift continues toward late-type stars, or even if it becomes convective redshift, as some indirect measurements suggest (Kürster et al. 2003).

Regarding general active region properties, measurements of spot sizes and locations have been made using the Doppler imaging technique (Vogt & Penrod 1983), obtaining filling factors that reach ∼10% of the stellar surface (Strassmeier 2009), or even larger, as were found studying magnetic regions with Zeeman-Doppler imaging (Donati et al. 1997; Morin et al. 2008). Other techniques such as light-curve inversion (Messina et al. 1999; Berdyugina et al. 2002) can be used to retrieve spot sizes and contrast temperatures, although with this method the determination of spot temperature is strongly correlated with spot size. However, this limitation can be overcome by analyzing light curves covering a wide range of photometric bands (Mallonn et al. 2018; Rosich et al. 2020). Modeling of photometric variations of late-type active stars has revealed that cool starspots are often quite large, covering up to 20% of the stellar surface (Berdyugina 2005). Regarding spot contrast temperatures, Berdyugina (2005) gave a representative sample of measurements suggesting values decreasing from ∼2000 K for late F- and G-type stars to ∼200 K for mid-M dwarfs. It should be noted that this work used a very limited and heterogeneous sample of stars, particularly M dwarfs, and combined spot temperatures determined from different methods, some of them prone to systematic biases and degeneracies.

In this paper, we demonstrate that the `StarSim` stellar activity model code (Herrero et al. 2016; Rosich et al. 2020) can provide stringent constraints on the properties of spots. In particular, a simultaneous fit to light and RV curves for several wavelength bands allows us to break the degeneracy between the spot coverage area and the temperature contrast, as well as to analyze the convective shift, providing a novel approach to measure this parameter. The chromatic index (CRX) introduced by Zechmeister et al. (2018) in the context of the CARMENES survey[1] (Calar Alto high-Resolution search for M dwarfs with Exo-earths with Near-infrared and optical Échelle Spectrographs; Quirrenbach et al. 2016, 2018), which measures the dependence of the radial velocity on wavelength, is ideally suited to the study of stellar activity effects. This index is defined as the slope of a linear fit to the RV as a function of the central wavelength logarithm of each order in a cross-dispersed échelle spectrum at each time step. Its use as an activity indicator relies on the wavelength dependence of photospheric heterogeneities because of the temperature contrast (Barnes et al. 2011; Jeffers et al. 2014). This dependence generally causes a decrease in the activity-induced RV variations toward the red-

dest orders (Desort et al. 2007), although strong magnetic fields may also have a large impact at longer wavelengths due to the Zeeman effect (Reiners et al. 2013; Shulyak et al. 2019).

In Sect. 2, we describe the model that we used to simulate time series of a rotating star with active regions, and we analyze which photospheric parameters play an important role. In Sect. 3, we present the spectroscopic and photometric observations of the active star YZ CMi and the results of the modeling of the spot parameters. Finally, in Sect. 4, we compare our results with previous parameter estimations using other methods and present our conclusions.

2. Modeling a spotted rotating star with `StarSim`

2.1. The `StarSim` model

`StarSim` is a sophisticated model used for simulating the effects of stellar spots on light and radial velocity curves. It allows us to generate precise synthetic photometric and spectroscopic time-series data of a spotted rotating photosphere. We briefly introduce the key aspects of the model here, but we refer the reader to Herrero et al. (2016) for a detailed description. The model is based on the integration of the spectral contribution of a fine grid of surface elements.

Synthetic PHOENIX spectra of different temperatures (Husser et al. 2013) are assigned to each of the surface elements, with a different temperature depending on the properties of the region (quiet photosphere, spot, or facula), and Doppler-shifted according to the projected velocity of the surface element. Photometric light curves or RVs are then computed by integrating all surface elements. To speed up the computation of RVs and other spectral indices related to the cross-correlation function (CCF), `StarSim` initially generates the CCFs produced from the spectrum of a single photosphere, spot, and facular element, and then integrates the entire visible surface using CCFs instead of spectra. A slow rotator template or a user-defined mask of spectral lines can be used to calculate the CCFs. Then, the contribution from each surface element is adjusted for the limb darkening computed from Kurucz ATLAS9 models (Kurucz 2017) at the specific angle with respect to the line of sight. `StarSim` defines the facular elements as circular regions around spots, whose area is controlled by the facula-to-spot area ratio. To properly account for the center-to-limb variations of convection effects in active regions, `StarSim` subtracts the bisector of the CCFs computed from the original PHOENIX spectra and then adds the bisector computed from CIFIST 3D models of a Sun-like star (Ludwig et al. 2009). The program also allows the adding of an arbitrary extra convective shift (blueshift or redshift) to the bisector of the CCFs corresponding to regions covered with spots or faculae. Finally, RV values are determined from the CCF at each epoch, which takes into account the distribution of spots and faculae and their properties, by fitting a Gaussian function.

Several stellar input parameters can be set in `StarSim`, such as the effective temperature of the star, the spot temperature, the position, size, and number of active regions, the convective shift, the stellar rotation period, the radius of the star, its surface gravity, and the inclination of the stellar spin axis with respect to the line of sight. Furthermore, one can select the wavelength range and compute time-series data of the photometry, RV, and CCF parameters.

To calculate the CRX parameter, we simulated RV curves for different wavelength ranges and measured their wavelength dependence. For this study, we used wavelength ranges matching those of the CARMENES visual channel échelle orders (i.e., 61

---

orders from 520 to 960 nm, Quirrenbach et al. 2016, 2018) to be consistent with our observational data. However, following Zechmeister et al. (2018), to compute the simulated CRX, we used the 40 orders (échelle orders 68 to 108) where the signal-to-noise ratio of the spectra is the highest, and thus observational RVs have lower uncertainties. The CRX is then computed as the slope of a linear fit to the RV as a function of the logarithm of the central wavelength of each order.

2.2. Dependence on photospheric parameters

To study the dependence of the RV and CRX time series on the properties of active regions, we ran several simulations considering a rotating spotted star. For simplicity, we assumed a single circular spot on the photosphere, and tested different values for the ratio of stellar surface covered by the spot (filling factor, ff), the temperature difference between the photosphere and the spot ($\Delta T \equiv T_{\mathrm{ph}} - T_{\mathrm{sp}}$), and the convective shift (CS). As explained in Sect. 2.1, StarSim introduces the influence of convective motions by adding a solar-like bisector to the CCF of each surface element. Thus, the solar convective blueshift is used as a reference. As an estimation of its absolute value, in our case a solar blueshift of $300\,\mathrm{m\,s^{-1}}$ (Dravins et al. 1981; Cavallini et al. 1985; Löhner-Böttcher et al. 2018) was subtracted from all CS values shown in this work. Therefore, the absolute values of CS given in this work have a dependence on the precise determination of the convective blueshift from CIFIST 3D models.

Stellar parameters such as effective temperature, surface gravity, and metallicity also have an impact on the RV and CRX time series due to their effects on stellar spectra. Besides this, the rotation of the star, its inclination, the latitude of the spot, and the presence of faculae do also play a role. However, these stellar parameters can be determined from fits to high-resolution spectra or through independent data. For this reason, we focus only on the impact of the properties of spots on RV and CRX time series.

For our simulations, we considered the case of a mid-M dwarf star approximately matching the properties of YZ CMi, which we use as a case study to compare with real observations later in Sect. 3. We fixed the stellar photospheric effective temperature to a value of 3100 K, the stellar surface gravity to $\log g = 5.0$, and we adopted solar metallicity. We assume an inclination of the rotation axis of $i = 90\,\mathrm{deg}$ (edge-on), and we introduce a spot on the equator, with no evolution and no differential rotation. The facula-to-spot area ratio was set to zero is as commonly found for active M-dwarf stars (Herrero et al. 2016; Mallonn et al. 2018; Rosich et al. 2020), and also as suggested by convection in magnetohydrodynamic simulations (Beeck et al. 2011, 2015).

Figure 1 illustrates the outcome of the simulations as a function of ff, ΔT and CS for RV and CRX. The bottom panels show that the CRX is strongly anti-correlated with the RV. As other authors have previously shown for the case of the bisector span (see, e.g., Boisse et al. 2011; Figueira et al. 2013), the CRX-RV anti-correlation is not a straight line, but it shows a lemniscate-like structure. The left panels in Fig. 1 show that varying ff mainly produces a change in the amplitude of both the RV and CRX time series, which in turn changes the scale of the correlation but preserving its slope and shape. The middle panels display the effect caused by different values of ΔT. This parameter has a much higher impact on the amplitude of the RV curve than on the CRX, producing a significant change in the slope of the correlation. Finally, CS changes the phase at which the RV peaks, and only slightly alters the asymmetry between

maximum and minimum of both the RV and CRX. This change in phase does not produce any change in the scale and slope of the RV-CRX correlation, but it has a significant imprint on its shape.

The different effects of stellar spot parameters on RV and CRX data can be understood by considering the main sources of variability, which are: (i) the flux effect caused by the contrast between inhomogeneities and the immaculate photosphere (Dumusque et al. 2014), and (ii) the inhibition of convection in active regions (Dravins et al. 1981; Stein et al. 1992; Chabrier et al. 2007). Both effects cause periodic variations of the measured RV of spotted stars. However, their dependence on rotation phase (or time) is different (see, e.g., Fig. 7 in Herrero et al. 2016). The flux effect vanishes when the spot is facing the observer (central phase) because the spot covers equivalent surface areas moving toward and away from the observer, hence, the net effect is canceled. Besides this, the flux effect is antisymmetric with respect to this point, meaning it causes an RV maximum when the spot crosses the hemisphere approaching the observer, and a minimum on the other side. On the other hand, the convection effect is maximal at the central phase, when the projected filling factor of the spot is largest, and the RV variability is symmetric with respect to this point. The difference between both effects produces a phase shift of the RV peaks for different wavelengths, causing the ∞ shape of the CRX-RV correlation, which becomes asymmetric depending on the parameters. The top-right panel in Fig. 1 shows that the phase shifts of RV time series are dominated by CS, while CRX remains almost unaffected (middle-right panel). The peak-to-peak amplitudes of both observables are mainly determined by the size and the temperature of the spot. This makes the analysis of chromatic radial velocities a unique tool to constrain CS, by simultaneously fitting the peak-to-peak amplitude and the phase shift of RV and CRX time series.

3. Fitting chromatic radial velocities of YZ CMi

3.1. The active star YZ CMi

The star YZ CMi (GJ 285) is a young star belonging to the β Pictoris moving group (Alonso-Floriano et al. 2015, and references therein). Its main properties are listed in Table 1. Maanen (1945) first announced the BY Dra-type photometric variability of the star, which was also classified as a flaring star by Lippincott (1952), showing UV Cet-type flares. Several flaring events were reported later (Andrews 1966; Sanwal 1976; Zhilyaev et al. 2011). A rotation period of 2.77 d from photometric variations was reported by Chugainov (1974) and confirmed by Pettersen et al. (1983). Recent estimations of the rotation period yielded very similar values (2.7758 ± 0.0006 d and 2.776 ± 0.010 d, Morin et al. 2008; Díez Alonso et al. 2019, respectively). Bondar' et al. (2019) found an activity cycle of 27.5 ± 2.0 yr, estimated from more than 80 years of archival photometric observations, with peak-to-peak variations of $0.2-0.3$ mag. Estimations of the effective temperature of YZ CMi range from 3045 K (from synthetic spectra fitting; Rojas-Ayala et al. 2012) to 3600 K (from spectral color indices; Zboril 2003).

The variability of the star has been extensively studied. The large color excess of YZ CMi indicates the presence of cool spots covering a large fraction of its surface. Zboril (2003) computed spot solutions from light curves taken in different seasons, and found a typical spot coverage between 10% and 25% of the surface, resulting from a single spot at a co-latitude $\sim 15-35$ deg from the pole and temperature ~ 500 K cooler than the
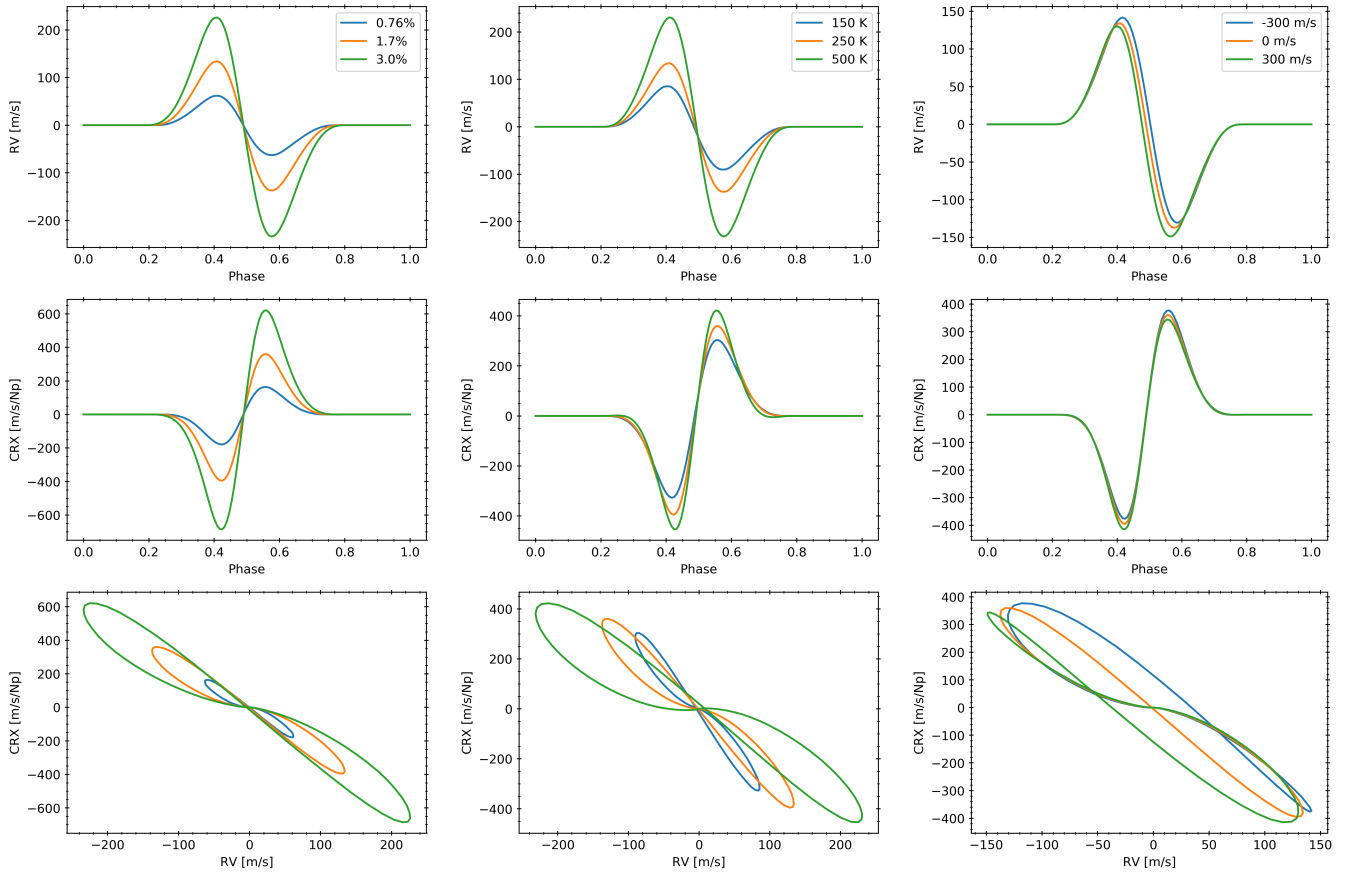
Fig. 1. Effect of properties of stellar spots on the RV (*top panels*) and CRX (*middle panels*) phase curves and on the RV-CRX correlation (*bottom panels*) for a mid-M dwarf. Simulations of varying ff (*left panels*), ΔT (*middle panels*), and CS (*right panels*) are shown while keeping the other parameters constant to a set of reference values. These reference values are 1.7% for the filling factor, 250 K for ΔT, and 0 m s^{-1} for CS. We note the different vertical scale in each plot, and that the horizontal axes are different in the *bottom panels*.

surrounding photosphere, all assuming an inclination ranging from 60 deg to 75 deg. Similarly, Alekseev & Kozhevnikova (2017) used 11 epochs of observations over 30 years of broadband photometry to compute the spottedness of YZ CMi. The authors assumed an effective temperature of 3300 K and an inclination of $i = 60$ deg, obtaining two belts of spots 210 ± 70 K cooler than the photosphere, which were mainly located at latitudes of $12-15$ deg, and covering up to 38% of the stellar surface. Using Zeeman-Doppler imaging and 25 spectropolarimetric observations taken between 2007 and 2008, Morin et al. (2008) found that the visible pole is covered by a large spot, with strong axisymmetry in the magnetic energy modes, hinting toward a non-visible spot at the other hemisphere. Morin et al. (2008) also inferred negligible differential rotation (0.0 ± 1.8 m rad d^{-1}).

We homogeneously derived the bolometric luminosity L and effective temperature $T_{\rm eff}$ of YZ CMi using broadband photometry in 17 passbands, from optical blue $B_{\rm T}$ (*Tycho*-2, Høg et al. 2000) to mid-infrared $W4$ (AllWISE, Cutri et al. 2013). None of the measurements used, especially at the bluest passbands, seemed to be affected by strong flaring activity. To determine L and $T_{\rm eff}$, we performed fits to the spectral energy distribution (SED), employing the BT-Settl CIFIST theoretical grid of models (Baraffe et al. 2015) and the Virtual Observatory SED Analyzer (VOSA, Bayo et al. 2008). The procedure is described in detail in Cifuentes et al. (2020). We took into account the long-term photometric variability of YZ CMi in the blue optical by re-running the SED fitting at the brightness maximum and minimum. For that, we were very conservative and used the largest reported variability amplitude of 0.3 mag in the B band (Bondar & Katsova 2018), over a scale of decades, to recompute extreme values of bolometric luminosity. We approximately extrapolated such amplitudes to 0.2 mag in the red optical, 0.1 mag in the near infrared, and 0.05 mag in the mid infrared, as observed in multiband photometric monitoring of very active M dwarfs (e.g., Caballero et al. 2006). The corresponding L and $T_{\rm eff}$ uncertainties of YZ CMi are thus larger than for invariable field M dwarfs of similar brightness. The radius was calculated using Stefan-Boltzmann's law following Schweitzer et al. (2019) and propagating the uncertainties in L and $T_{\rm eff}$.

We estimated the inclination of the stellar spin axis from the radius, the rotation period and the projected velocity, which yielded $i = 36^{+17}_{-14}$ deg. The uncertainty was computed from 10^6 random resamplings of the input parameters according to their quoted uncertainties. The lower inclination value that we find, contrary to other studies (Zboril 2003; Morin et al. 2008; Alekseev & Kozhevnikova 2017), arises from the different projected velocity and stellar radius used. In particular, projected rotational velocities of 5.0 and 6.5 km s^{-1} (Delfosse et al. 1998; Reiners & Basri 2007) and stellar radii of 0.30 and 0.37 $R_\odot$ (Delfosse et al. 2000; Pettersen 1980) were reported. Based on CARMENES data, Reiners et al. (2018) reported $v \sin i = 4.0 \pm 1.5$ km s^{-1}, and we find a stellar radius of 0.369 $R_\odot$ following Schweitzer et al. (2019). The resulting parameters are listed in Table 1.

Table 1. Basic properties of YZ CMi.

Parameters	Values	Ref.
GJ	285	GJ79
Karmn	J07446+035	AF15
α (J2000)	07:44:40.17	*Gaia* DR2
δ (J2000)	+03:33:08.9	*Gaia* DR2
d [pc]	5.9874 ± 0.0021	*Gaia* DR2
G [mag]	9.6807 ± 0.0010	*Gaia* DR2
J [mag]	6.581 ± 0.024	2MASS
Sp. type	M4.5 V	PMSU
$T_{\rm eff}$ [K]	3100 ± 50	This work
$\log g$ [cgs]	5.0 ± 0.5	Lep13
$L_\star$ [$10^{-4}\,L_\odot$]	113^{+17}_{-14}	This work
$R_\star$ [$R_\odot$]	$0.369^{+0.027}_{-0.055}$	This work
pEW(Hα) [Å]	-7.097 ± 0.023	Jef18
$v \sin i$ [km s^{-1}]	4.0 ± 1.5	Rei18
$P_{\rm rot}$ [d]	2.776 ± 0.010	DA19
i [deg]	36^{+17}_{-14}	This work

References. 2MASS: Skrutskie et al. (2006); AF15: Alonso-Floriano et al. (2015); DA19: Díez Alonso et al. (2019); *Gaia* DR2: Gaia Collaboration (2016, 2018); GJ79: Gliese & Jahreiß (1979); Jef18: Jeffers et al. (2018); Lep13: Lépine et al. (2013); PMSU: Hawley et al. (1996); Rei18: Reiners et al. (2018).

The selection of this target for analysis of its stellar activity properties was based on two main points: (i) it is one of the M-dwarf stars with the strongest activity-induced RV variability within the CARMENES survey, with peak-to-peak amplitudes of $\sim$300 m s^{-1}, and (ii) it is also one of the stars with the strongest RV-CRX correlation (Tal-Or et al. 2018), which could be indicative of large spots.

3.2. CARMENES observations

YZ CMi is one of the targets of the CARMENES survey (Reiners et al. 2018). CARMENES is a double-channel spectrometer of which the aim is the discovery of exoplanets orbiting M-dwarf stars. It obtains high-resolution spectra of stars simultaneously in two different wavelength ranges, one in the red-visible and another one in the near-infrared, covering from 520 to 960 nm and from 960 to 1710 nm, respectively. Besides radial velocities and some commonly used spectral indices, the CARMENES `serval` pipeline Zechmeister et al. (2018) also computes the CRX. YZ CMi was observed between 2016 and 2018 at 49 epochs. To mitigate the possible effects of spot evolution, an observational campaign to sample all rotational phases was conducted between September 2016 and May 2017, yielding a total of 27 valid observations, which are used in this work. Figure 2 displays the RV and CRX time series, and all used data are available in Table A.1. Figure 3 shows the same measurements, but phase folded to the stellar rotation period of 2.776 d (Díez Alonso et al. 2019). RV and CRX are anti-correlated, as was expected given the results of the simulations in Sect. 2.2.

3.3. Photometric data

We also secured photometric monitoring of YZ CMi contemporaneously to RV observations. We obtained 460 photometric measurements using a Johnson *R* filter with the Telescopi *Joan Oró* (TJO), located at the Montsec Astronomical Observatory in Lleida, Spain. The TJO is a fully-robotic 0.8 m Ritchey-Chrétien
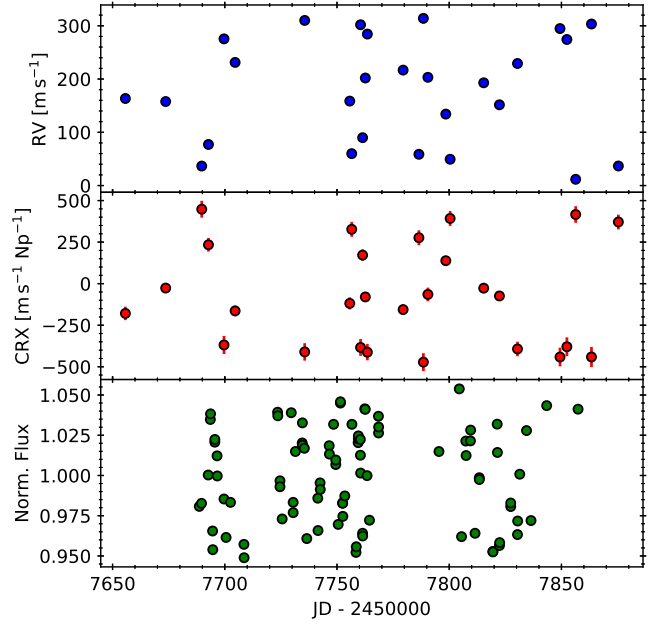
Fig. 2. RV (*top*), CRX (*middle*), and photometric (*bottom*) time series of YZ CMi obtained with CARMENES and TJO.
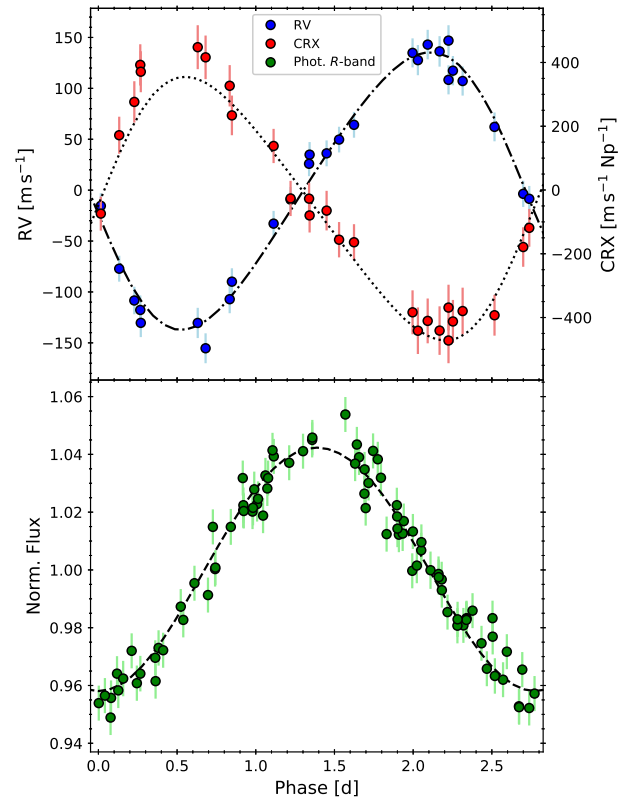
Fig. 3. Phase-folded RV (blue circles), CRX (red circles), and photometric (green circles) data obtained for YZ CMi. *Top panel*: the left and right vertical axes correspond to RV and CRX, respectively. The best models that simultaneously fit the three datasets are shown as dash-dotted (RVs) and dotted (CRX) lines, and they correspond to the values found in Table 2. The error bars correspond to the quadrature addition between observational uncertainties and the fit jitter parameter for each dataset.

telescope. The photometric data were obtained with the MEIA2 instrument, an Andor $2k \times 2k$ CCD camera with a plate scale of

0.36 arcsec per pixel. We gathered these observations between October 2016 and April 2017. After rebinning the data with a cadence of 30 min, we performed a 2.5σ-clipping to the residuals after a sinusoidal fit, in order to remove outliers due to flaring events, which resulted in a total of 89 photometric epochs. The bottom panels in Figs. 2 and 3 display the resulting photometric data.

3.4. Surface distribution of the active regions

Before analyzing the impact of the size and the temperature of spots and the convective shift on the RV and CRX time series of YZ CMi, we needed to estimate the distribution of active regions on the stellar photosphere, particularly their latitude. Although light curves are not strongly sensitive to the latitude of active regions, including RV data in the analysis does solve this problem. This is especially true in the case of YZ CMi, for which a constraint on the inclination of the spin axis is available. For this purpose, we made use of the implementation of the inverse problem in `StarSim`, which allows the fitting of the spot distribution that best matches light or radial velocity curves (Rosich et al. 2020). This new implementation solves the inverse problem by using several small active elements on the star, which may be concentrated to reproduce spot groups. We used the stellar input parameters from Table 1, and we estimated the latitude of active regions from the observed RV and photometric time series assuming different temperature contrast values in the range $\Delta T = 50-400$ K. We found that, while the size of active elements showed some correlation with their temperature contrast, their latitudes were always in the range $75-81$ deg. The inversion of the RVs using a model with 20 active surface elements resulted in all of them concentrated around the same region. For that reason, and to speed up and simplify the fitting procedure, we decided to further model the data with a larger single non-evolving circular spot located at a latitude of $\lambda_{\rm spot} = 78$ deg.

3.5. Fit spot parameters

Assuming the spot model described above, we analyzed the impact of ΔT, ff, and CS on the RV, CRX, and photometric time series of YZ CMi, and we determined the values that best fit all datasets simultaneously. The simulation of RV data using `StarSim` involves the computation of the CCF for each surface element of the star, a process that is computationally expensive. Therefore, we decided to fix the stellar parameters to those listed in Table 1, and compared our simulations with the observed RV, CRX, and light curves on a grid of the ΔT-ff-CS parameter space. To explore the parameter domain, the likelihood of the `StarSim` models given the observed datasets was first computed on a coarse grid, with 20 K, ~3.5%, and 50 m s^{-1} steps in ΔT, ff, and CS, respectively. We subsequently defined a finer grid with step sizes divided by four to explore the regions with higher likelihood values. The likelihood at each grid point was computed by also considering an offset to the RVs ($\gamma_{\rm RV}$), and a global reference time shift to the RVs, CRX, and photometry ($\Delta t_{\rm ref}$), relating the central longitude of the star to the rotational phase. Finally, we also added jitter terms ($\sigma_{\rm RV}$, $\sigma_{\rm CRX}$, $\sigma_{\rm phot}$) to the RVs, CRX, and photometry, respectively, to account for the limitations of a single-spot model. These jitter terms are added in quadrature to the corresponding uncertainties to evaluate the likelihood function, as defined in Baluev (2009). The final model likelihood value reported is the sum of the individual likelihood values obtained for the RV, CRX, and photometry datasets.

Figure 4 displays the log-likelihood difference with respect to the best model, $\Delta \ln L$, in the ΔT–ff plane for different values of CS. Dotted symbols correspond to the inspected grid of parameters, which is finer in the regions corresponding to the best fit of observations. The $\Delta \ln L$ corresponding to the RV, CRX, and photometry fits are independently plotted with blue, red, and green contours, respectively, while black contours indicate the joint values. Although photometric fits are independent of the convective shift, they constrain the ff and ΔT correlation very well. On the other hand, both RV and CRX are much more sensitive to CS changes, which breaks the strong ff–ΔT correlation present in the photometry fits. The different panels in Fig. 4 show that, in spite of the similar solution ranges for ff and ΔT, the CRX provides a stringent constraint on the upper value of CS. As a further check, we ran a test excluding the CRX dataset and we found that the uncertainty on the value of CS increases by a factor of ~2. Thus, although the filling factor and the spot temperature contrast can be determined from a simultaneous fit to the RV and photometry only, the CRX provides valuable information to constrain the convective shift. Overlap between photometry, RV, and CRX $\Delta \ln L$ surfaces (i.e., best simultaneous fit to all datasets) occurs around $CS \sim 50$ m s^{-1}, suggesting a global convective redshift for YZ CMi. We note, however, that although the best solutions yield convective redshift, there are acceptable solutions ($\Delta \ln L < 10$) located in the convective blueshift region.

To estimate the optimal parameters fitting the CARMENES RV and CRX data and the TJO light curve, along with their uncertainties, we interpolated the $\ln L$ hypersurface over the grid used to search for the best solution (ΔT, ff, CS), also including the adjusted parameters ($\gamma_{\rm RV}$, $\Delta t_{\rm ref}$, $\sigma_{\rm RV}$, $\sigma_{\rm CRX}$, and $\sigma_{\rm phot}$). For this purpose, we used a Gaussian process model based on a squared exponential covariance function, similarly to the likelihood inference explained by Fleming & VanderPlas (2018). Compared to a linear interpolation, this interpolator produces smoother profiles, and can also infer maxima outside the evaluated points. We maximized the likelihood using the Powell method inside the `scipy.optimize` Python package. Formal uncertainties were derived from the covariance matrix, computed from the Hessian evaluated at the maximum. Table 2 lists the parameters of the best fitting model, together with the minimum and maximum values found using other stellar parameters (see below). The RV and CRX fits using these parameters are shown in the top panel of Fig. 3, while the bottom panel shows the fit to the photometry. Figure 5 illustrates the correlation between RV and CRX, showing that the cyclic evolution is well reproduced by the `StarSim` model. Comparing Fig. 5 with the bottom panels in Fig. 1, YZ CMi data show better consistency with the RV-CRX correlation with negative CS than with the ∞ shape corresponding to a null CS effect. This correlation can in fact be used as a clear observable of convective blueshift or redshift thanks to the asymmetry introduced toward positive or negative velocities, respectively. Although the bottom-left panel in this figure shows a twisted loop, this also depends on the filling factor and temperature of spots. For YZ CMi, the CS is ~6 times smaller than in the simulations in Fig. 1, but the filling factor is also ~6 times larger, causing the untwisted loop.

The uncertainties of the spot parameters may be underestimated, because we assumed fixed stellar properties. We remind the reader that this is due to the computational effort needed to run the RV simulations, which prevents us from exploring solutions also including stellar properties as free parameters. To study the impact on the parameter uncertainties, we repeated the process to simultaneously fit the RV and CRX data considering
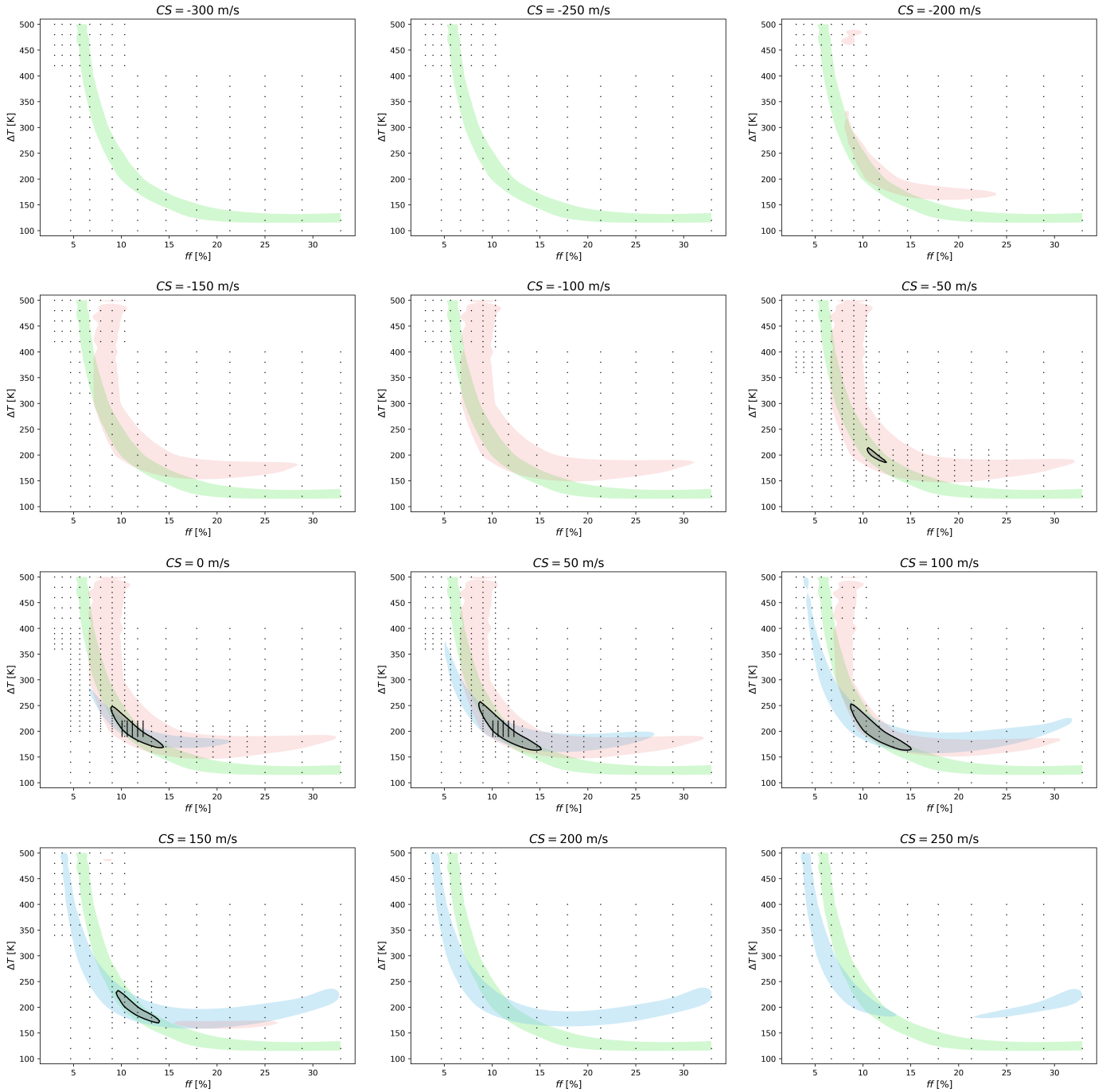
Fig. 4. $\Delta \ln L$ contour plots corresponding to the RV (blue), CRX (red), photometry (green), and combined (black) fits for different CS slices. The colored regions are within a $\Delta \ln L = 10$ with respect to the best fit among all the CS slices. Black dots indicate the points of contrast temperature and filling factor used to sample the parameter space.

a set of values for the effective temperature ($T_{\rm eff}$) of YZ CMi and its spin axis inclination (i) spanning the reported uncertainties in Table 1. These are the parameters identified to potentially induce changes on the simulated RV. A different $T_{\rm eff}$ could potentially change the temperature and size of spots required to reproduce the observations, while a change in i may also have an impact on the latitude and size of the spots and their imprint on RVs. Table 3 lists the results of the fits for the set of $T_{\rm eff}$ and i values used for this purpose. All solutions are statistically equivalent ($\Delta \ln L < 10$), except for the simulations with an inclination of 52.5 deg, which start to fail at reproducing the CRX,

as indicated by their relatively higher jitter. Additionally, the fit parameters span a wider range than the formal uncertainties previously reported for fixed stellar parameters. We list these additional systematic uncertainties caused by the error bars of the stellar properties in the third column of Table 2.

4. Discussion and conclusions

Our model for YZ CMi indicates that this active star has at least a prominent spot with a filling factor in the ~9.5−13.3% range. The value that we found is compatible with previous values in

Table 2. Best fitting parameters and ranges introduced by the uncertainties on T_{eff} and i to the YZ CMi RV, CRX, and photometric datasets.

Parameters	Best model	Range	
		Min.	Max.
ff [%]	11.16 ± 0.66	9.53	13.25
ΔT [K]	199.7 ± 9.6	178.6	273.4
CS [m s^{-1}]	56 ± 37	7	237
Δt_{ref} [d]	1.9879 ± 0.0078	1.9735	2.0043
γ_{RV} [m s^{-1}]	-166.8 ± 2.5	-169.5	-163.6
σ_{RV} [m s^{-1}]	11.2 ± 2.2	8.5	17.7
σ_{CRX} [m s^{-1} Np^{-1}]	47 ± 14	33	125
σ_{phot} [$\times 10^{-3}$]	6.00 ± 0.47	5.45	6.67
$\ln L$	70.8	52.0	72.8
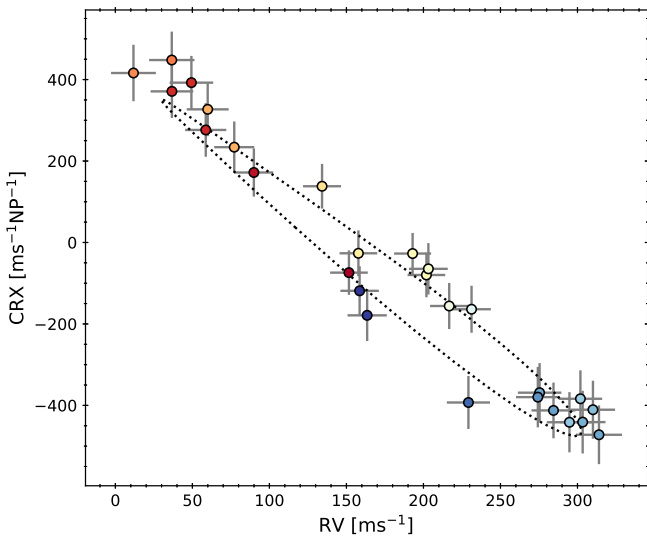
Fig. 5. Best fit model (dotted line) compared to observations (symbols) in the RV-CRX parameter space. The colors of the symbols indicate the rotation phase at which each observation was made.

the literature by Zboril (2003) and Alekseev & Kozhevnikova (2017), who suggested filling factors of 10−25% and 10−38%, respectively. The significantly broader (and less precise) ranges reported in these works most likely arise from the use of only light curves, which, as we showed in Fig. 4, produce a strong degeneracy in the ff–ΔT plane. However, because of the different adopted stellar inclinations, contrast temperatures, and spot models used in these two works, caution should be taken when performing comparisons. They used stellar inclinations of 60−70 deg, Zboril (2003) fixed the contrast temperature to 500 K, and Alekseev & Kozhevnikova (2017) used two spot belts. Furthermore, the spot size and latitude that we estimate are consistent with a spot covering a large fraction of the visible pole, in agreement with the results obtained by Zeeman-Doppler imaging (Morin et al. 2008).

From our analysis, we constrain the temperature difference between the photosphere and the spot to a 1σ confidence range of ∼179−273 K. These values are in close agreement with the ΔT results by Alekseev & Kozhevnikova (2017), and consistent with the commonly used empirical calibration by Berdyugina (2005) and Andersen & Korhonen (2015). However, our results are better constrained due to the simultaneous fit of photometric,

RV, and CRX time series covering several wavelength bands that allow the breaking of the spot temperature and the filling factor degeneracy. Furthermore, the scarcity of spot crossing events on the ∼4000 M dwarfs in the *Kepler* catalog could be indicative of a low contrast ratio for the spots on the photospheres of these stars (i.e., smaller ΔT), assuming a heterogeneous distribution of spots (Andersen & Korhonen 2015). The study of multiband photometric observations also points toward a smaller temperature difference for late-type stars than for solar-like stars (Mallonn et al. 2018).

We note that differences in temperature and filling factors available in the literature may also be due to the evolution of stellar activity features. For instance, as a further check, we compared our simulations with the two-minute cadence photometry available for YZ CMi from the Transiting Exoplanet Survey Satellite (TESS, Ricker et al. 2015), obtained between January and February 2019, two years after our CARMENES dataset. Figure 6 shows this light curve along with the model corresponding to the best fitting parameters listed in Table 2, and with the range defined by all the models in Table 3. Although the overall aspect is similar, the TESS light curve has a lower amplitude compared to our models. This difference can be reproduced by reducing the filling factor by ∼3.5% or with a temperature contrast 40 K lower, and may be due to the time evolution of spots. Interestingly, the phase and shape of the modulation is consistent with our model, which may point to a long-lived active region that does not change its position on the stellar surface significantly.

Finally, the simultaneous fit to RV, CRX, and photometric time series results in a global convective shift for YZ CMi in the range between +7 and +237 m s^{-1}, in contrast with the value of −300 m s^{-1} estimated for the Sun. Interestingly, this result means that the convection effect produces a net redshift, not a blueshift, although this result must be taken with caution given the large uncertainty. Such a possibility was already suggested by Kürster et al. (2003) based on the anti-correlation between the Hα line strength and the RV for Barnard's Star, indicating an increase in the blueshift when the coverage of the star with plage regions increases. Similar conclusions are suggested by 3D hydrodynamic simulations, which also predict a very small net convective blueshift for late K-type stars, but they increase with the effective temperature of the star until they reach a blueshift of 300 m s^{-1} for F-type dwarfs (Allende Prieto et al. 2013). Meunier et al. (2017) described a similar trend from the estimation of the convective blueshift using Fe and Ti lines of 360 F7–K4 stars. For the particular case of M-dwarf stars, magnetohydrodynamic simulations suggest that convective motions are less vigorous and that the average granule velocity shift is also smaller (Beeck et al. 2013a,b).

To conclude, the results of our analysis reveal that a simultaneous fit to light and RV curves for several wavelength bands represents a novel approach to estimating not only properties of stellar activity, such as the spot filling factor and temperature difference (breaking their degeneracy), but also the shift of radial velocities due to convective motions. From the particular case of YZ CMi presented here, and its comparison to the Sun, we conclude that the absolute convective shift may be reversed toward redshift for M-dwarf stars. Finally, the chromatic index is not affected by the Keplerian orbital motion of exoplanets seen in the radial velocity, and can therefore provide vital information to disentangle exoplanet signals from stellar activity effects.

Table 3. Best fit parameters for every $T_{\rm eff}$–i set of models.

Model			Best fit parameters									ln L
$T_{\rm eff}$ (K)	i (deg)	$\lambda_{\rm spot}$ (deg)	$f\!f_{\rm max}$ (%)	ΔT (K)	CS (m s^{-1})	$\Delta t_{\rm ref}$ (d)	$\gamma_{\rm RV}$ (m s^{-1})	$\sigma_{\rm RV}$ (m s^{-1})	$\sigma_{\rm CRX}$ (m s^{-1} Np^{-1})	$\sigma_{\rm phot}$ ($\times 10^{-3}$)	
3050	21.5	73	11.66 ± 0.78	196 ± 12	49 ± 39	1.9932 ± 0.0080	−167.0 ± 2.4	10.9 ± 2.0	50 ± 13	5.93 ± 0.46	71.4
3050	30.0	77	11.89 ± 0.72	188.5 ± 9.9	57 ± 39	1.9930 ± 0.0080	−167.0 ± 2.5	11.1 ± 2.1	49 ± 14	5.93 ± 0.46	71.1
3050	36.0	78	11.11 ± 0.67	194 ± 10	49 ± 39	1.9869 ± 0.0079	−166.8 ± 2.5	11.4 ± 2.3	48 ± 14	6.00 ± 0.47	69.9
3050	45.0	79	10.51 ± 0.71	210 ± 13	62 ± 24	1.9839 ± 0.0079	−166.8 ± 2.6	12.0 ± 2.3	60 ± 14	6.09 ± 0.48	63.8
3050	52.5	80	9.96 ± 0.43	249.7 ± 8.8	68 ± 61	1.9821 ± 0.0086	−166.6 ± 3.0	14.4 ± 3.3	84 ± 20	6.17 ± 0.50	52.0
3100	21.5	73	11.65 ± 0.48	202.3 ± 7.2	56 ± 37	1.9941 ± 0.0078	−167.0 ± 2.4	10.9 ± 2.0	50 ± 13	5.93 ± 0.46	71.6
3100	30.0	77	12.33 ± 0.92	190.5 ± 9.6	70 ± 37	1.9931 ± 0.0081	−167.1 ± 2.4	10.7 ± 2.0	49 ± 13	5.93 ± 0.46	71.9
3100 [a]	36.0 [a]	78 [a]	11.16 ± 0.66	199.7 ± 9.6	56 ± 37	1.9879 ± 0.0078	−166.8 ± 2.5	11.2 ± 2.2	47 ± 14	6.00 ± 0.47	70.8
3100	45.0	79	10.68 ± 0.63	214.7 ± 9.4	79 ± 22	1.9855 ± 0.0080	−166.8 ± 2.5	11.5 ± 2.3	61 ± 15	6.06 ± 0.48	64.8
3100	52.5	80	10.26 ± 0.67	257 ± 14	167 ± 61	1.9869 ± 0.0089	−166.9 ± 2.5	11.6 ± 2.2	103 ± 22	6.09 ± 0.49	53.3
3150	21.5	73	11.51 ± 0.90	212 ± 14	74 ± 39	1.9962 ± 0.0081	−167.0 ± 2.4	10.7 ± 1.9	55 ± 13	5.91 ± 0.46	70.7
3150	30.0	77	12.06 ± 0.74	201.0 ± 9.8	86 ± 35	1.9947 ± 0.0079	−167.0 ± 2.4	10.6 ± 1.9	49 ± 13	5.92 ± 0.46	72.8
3150	36.0	78	11.76 ± 0.81	200 ± 11	93 ± 32	1.9930 ± 0.0078	−167.0 ± 2.3	10.4 ± 1.9	49 ± 13	5.95 ± 0.46	72.4
3150	45.0	79	11.01 ± 0.86	215 ± 13	132 ± 39	1.9932 ± 0.0083	−166.9 ± 2.3	10.4 ± 2.0	64 ± 15	5.98 ± 0.47	67.1
3150	52.5	80	10.55 ± 0.46	253.0 ± 9.5	180 ± 57	1.9881 ± 0.0082	−167.0 ± 2.5	11.3 ± 2.4	91 ± 20	6.11 ± 0.49	56.3

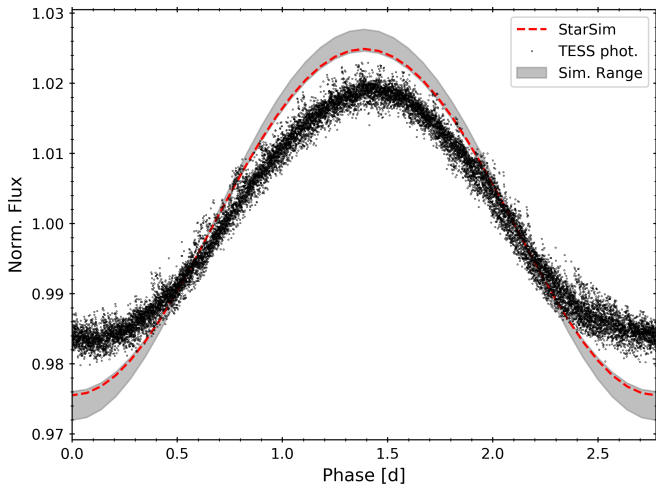**Notes.** [a] Stellar parameters used as the best model in Table 2.

Fig. 6. Phase-folded TESS photometric observations (black dots compared to the StarSim simulation (dashed line) using the best model values and the TESS-band filter. The gray shaded region corresponds to the range defined by all the best model simulations in Table 3.

References

Alekseev, I. Y., & Kozhevnikova, A. V. 2017, Astron. Rep., 61, 221
Allende Prieto, C., Koesterke, L., Ludwig, H. G., Freytag, B., & Caffau, E. 2013, A&A, 550, A103
Alonso-Floriano, F. J., Caballero, J. A., Cortés-Contreras, M., Solano, E., & Montes, D. 2015, A&A, 583, A85
Andersen, J. M., & Korhonen, H. 2015, MNRAS, 448, 3053
Andrews, A. D. 1966, PASP, 78, 324
Baluev, R. V. 2009, MNRAS, 393, 969
Baraffe, I., Homeier, D., Allard, F., & Chabrier, G. 2015, A&A, 577, A42
Barnes, J. R., Jeffers, S. V., & Jones, H. R. A. 2011, MNRAS, 412, 1599
Bayo, A., Rodrigo, C., Barrado Y Navascués, D., et al. 2008, A&A, 492, 277
Beeck, B., Schüssler, M., & Reiners, A. 2011, in 16th Cambridge Workshop on Cool Stars, Stellar Systems, and the Sun, eds. C. Johns-Krull, M. K. Browning, & A. A. West, ASP Conf. Ser., 448, 1071
Beeck, B., Cameron, R. H., Reiners, A., & Schüssler, M. 2013a, A&A, 558, A48
Beeck, B., Cameron, R. H., Reiners, A., & Schüssler, M. 2013b, A&A, 558, A49
Beeck, B., Schüssler, M., Cameron, R. H., & Reiners, A. 2015, A&A, 581, A42
Benedict, G. F., Nelan, E., McArthur, B., et al. 1993, PASP, 105, 487
Berdyugina, S. V. 2005, Liv. Rev. Sol. Phys., 2, 8
Berdyugina, S. V., Pelt, J., & Tuominen, I. 2002, A&A, 394, 505
Boisse, I., Bouchy, F., Hébrard, G., et al. 2011, A&A, 528, A4
Boisse, I., Bonfils, X., & Santos, N. C. 2012, A&A, 545, A109
Bondar, N. I., & Katsova, M. M. 2018, Geomagn. Aeron., 58, 910
Bondar', N. I., Gorbunov, M. A., & Shlyapnikov, A. A. 2019, in A Search for Cyclic Activity of Red Dwarfs Using Photometric Surveys, eds. D. O. Kudryavtsev, I. I. Romanyuk, & I. A. Yakunin, ASP Conf. Ser., 518, 180
Bonfils, X., Lo Curto, G., Correia, A. C. M., et al. 2013, A&A, 556, A110
Caballero, J. A., Martín, E. L., Zapatero Osorio, M. R., et al. 2006, A&A, 445, 143
Cavallini, F., Ceppatelli, G., & Righini, A. 1985, A&A, 150, 256
Chabrier, G., Gallardo, J., & Baraffe, I. 2007, A&A, 472, L17
Chugainov, P. F. 1974, Izvestiya Ordena Trudovogo Krasnogo Znameni Krymskoj Astrofizicheskoj Observatorii, 52, 3

Cifuentes, C., Caballero, J. A., Cortés-Contreras, M., et al. 2020, A&A, in press, https://doi.org/10.1051/0004-6361/202038295

Cutri, R. M., Wright, E. L., Conrow, T., et al. 2013, Explanatory Supplement to the AllWISE Data Release Products, Explanatory Supplement to the AllWISE Data Release Products

Delfosse, X., Forveille, T., Perrier, C., & Mayor, M. 1998, A&A, 331, 581

Delfosse, X., Forveille, T., Ségransan, D., et al. 2000, A&A, 364, 217

Desort, M., Lagrange, A.-M., Galland, F., Udry, S., & Mayor, M. 2007, A&A, 473, 983

Díez Alonso, E., Caballero, J. A., Montes, D., et al. 2019, A&A, 621, A126

Donati, J. F., Semel, M., Carter, B. D., Rees, D. E., & Collier Cameron, A. 1997, MNRAS, 291, 658

Dravins, D. 1999, in Stellar Surface Convection, Line Asymmetries, and Wavelength Shifts, eds. J. B. Hearnshaw, & C. D. Scarfe, ASP Conf. Ser., 185, 268

Dravins, D., Lindegren, L., & Nordlund, A. 1981, A&A, 96, 345

Dumusque, X., Boisse, I., & Santos, N. C. 2014, ApJ, 796, 132

Figueira, P., Santos, N. C., Pepe, F., Lovis, C., & Nardetto, N. 2013, A&A, 557, A93

Fleming, D. P., & VanderPlas, J. 2018, J. Open Source Softw., 3, 781

Gaia Collaboration (Prusti, T., et al.) 2016, A&A, 595, A1

Gaia Collaboration (Brown, A. G. A., et al.) 2018, A&A, 616, A1

Gliese, W., & Jahreiß, H. 1979, A&AS, 38, 423

Gray, D. F. 2009, ApJ, 697, 1032

Hanslmeier, A., Nesis, A., & Mattig, W. 1991, A&A, 251, 307

Hatzes, A. P. 2002, Astron. Nachr., 323, 392

Hawley, S. L., Gizis, J. E., & Reid, I. N. 1996, AJ, 112, 2799

Herrero, E., Ribas, I., Jordi, C., et al. 2016, A&A, 586, A131

Høg, E., Fabricius, C., Makarov, V. V., et al. 2000, A&A, 355, L27

Husser, T. O., Wende-von Berg, S., Dreizler, S., et al. 2013, A&A, 553, A6

Jeffers, S. V., Barnes, J. R., Jones, H. R. A., et al. 2014, MNRAS, 438, 2717

Jeffers, S. V., Schöfer, P., Lamert, A., et al. 2018, A&A, 614, A76

Kürster, M., Endl, M., Rouesnel, F., et al. 2003, A&A, 403, 1077

Kurucz, R. L. 2017, Astrophysics Source Code Library [record ascl:1710.017]

Lanza, A. F., Bonomo, A. S., & Rodonò, M. 2007, A&A, 464, 741

Lanza, A. F., Bonomo, A. S., Moutou, C., et al. 2010, A&A, 520, A53

Lépine, S., Hilton, E. J., Mann, A. W., et al. 2013, AJ, 145, 102

Lippincott, S. L. 1952, ApJ, 115, 582

Livingston, W., Wallace, L., Huang, Y., & Moise, E. 1999, in High Resolution Information on Granulation from Full Disk Fe Line Asymmetry, eds. T. R. Rimmele, K. S. Balasubramaniam, & R. R. Radick, ASP Conf. Ser., 183, 494

Löhner-Böttcher, J., Schmidt, W., Schlichenmaier, R., et al. 2018, A&A, 617, A19

Ludwig, H. G., Caffau, E., Steffen, M., et al. 2009, Mem. Soc. Astron. It., 80, 711

Maanen, A. V. 1945, PASP, 57, 216

Mallonn, M., Herrero, E., Juvan, I. G., et al. 2018, A&A, 614, A35

Marcy, G. W., & Butler, R. P. 1998, ARA&A, 36, 57

Messina, S., Guinan, E. F., Lanza, A. F., & Ambruster, C. 1999, A&A, 347, 249

Meunier, N., Desort, M., & Lagrange, A. M. 2010, A&A, 512, A39

Meunier, N., Mignon, L., & Lagrange, A. M. 2017, A&A, 607, A124

Morin, J., Donati, J. F., Petit, P., et al. 2008, MNRAS, 390, 567

Perger, M., García-Piquer, A., Ribas, I., et al. 2017, A&A, 598, A26

Pettersen, B. R. 1980, A&A, 82, 53

Pettersen, B. R., Kern, G. A., & Evans, D. S. 1983, A&A, 123, 184

Quirrenbach, A., Amado, P. J., Caballero, J. A., et al. 2016, in Ground-based and Airborne Instrumentation for Astronomy VI, Proc. SPIE, 9908, 990812

Quirrenbach, A., Amado, P. J., Ribas, I., et al. 2018, in Ground-based and Airborne Instrumentation for Astronomy VII, SPIE Conf. Ser., 10702, 107020W

Rajpaul, V., Aigrain, S., Osborne, M. A., Reece, S., & Roberts, S. 2015, MNRAS, 452, 2269

Reiners, A., & Basri, G. 2007, ApJ, 656, 1121

Reiners, A., Bean, J. L., Huber, K. F., et al. 2010, ApJ, 710, 432

Reiners, A., Shulyak, D., Anglada-Escudé, G., et al. 2013, A&A, 552, A103

Reiners, A., Zechmeister, M., Caballero, J. A., et al. 2018, A&A, 612, A49

Ricker, G. R., Winn, J. N., Vanderspek, R., et al. 2015, J. Astron. Telesc. Instrum. Syst., 1, 014003

Robertson, P., Mahadevan, S., Endl, M., & Roy, A. 2014, Science, 345, 440

Robertson, P., Endl, M., Henry, G. W., et al. 2015, ApJ, 801, 79

Rojas-Ayala, B., Covey, K. R., Muirhead, P. S., & Lloyd, J. P. 2012, ApJ, 748, 93

Rosich, A., Herrero, E., Mallonn, M., et al. 2020, A&A, in press, https://doi.org/10.1051/0004-6361/202037586

Saar, S. H., & Donahue, R. A. 1997, ApJ, 485, 319

Sanwal, B. B. 1976, Inf. Bull. Var. Stars, 1180, 1

Schweitzer, A., Passegger, V. M., Cifuentes, C., et al. 2019, A&A, 625, A68

Shulyak, D., Reiners, A., Nagel, E., et al. 2019, A&A, 626, A86

Skrutskie, M. F., Cutri, R. M., Stiening, R., et al. 2006, AJ, 131, 1163

Stein, R. F., Brandenburg, A., & Nordlund, A. 1992, in Magnet Convection (Invited Review), eds. M. S. Giampapa, & J. A. Bookbinder, ASP Conf. Ser., 26, 148

Strassmeier, K. G. 2009, A&ARv, 17, 251

Tal-Or, L., Zechmeister, M., Reiners, A., et al. 2018, A&A, 614, A122

Title, A. M., Tarbell, T. D., & Topka, K. P. 1987, ApJ, 317, 892

Vogt, S. S., & Penrod, G. D. 1983, PASP, 95, 565

Zboril, M. 2003, Astron. Nachr., 324, 527

Zechmeister, M., Reiners, A., Amado, P. J., et al. 2018, A&A, 609, A12

Zhilyaev, B. E., Tsap, Y. T., Andreev, M. V., et al. 2011, Kinemat. Phys. Celest. Bodies, 27, 154

1 Institut de Ciències de l'Espai (ICE, CSIC), Campus UAB, c/Can Magrans s/n, 08193 Bellaterra, Barcelona, Spain
e-mail: baroch@ice.cat

2 Institut d'Estudis Espacials de Catalunya (IEEC), c/ Gran Capità 2-4, 08034 Barcelona, Spain

3 Institut für Astrophysik, Georg-August-Universität, Friedrich-Hund-Platz 1, 37077 Göttingen, Germany

4 Centro de Astrobiología (CSIC-INTA), ESAC, Camino Bajo del Castillo s/n, 28692 Villanueva de la Cañada, Madrid, Spain

5 Landessternwarte, Zentrum für Astronomie der Universität Heidelberg, Königstuhl 12, 69117 Heidelberg, Germany

6 Instituto de Astrofísica de Andalucía (IAA-CSIC), Glorieta de la Astronomía s/n, 18008 Granada, Spain

7 Hamburger Sternwarte, Gojenbergsweg 112, 21029 Hamburg, Germany

8 Homer L. Dodge Department of Physics and Astronomy, University of Oklahoma, 440 West Brooks Street, Norman, OK 73019, USA

9 Instituto de Astrofísica de Canarias, Vía Láctea s/n, 38205 La Laguna, Tenerife, Spain

10 Departamento de Astrofísica, Universidad de La Laguna, 38026 La Laguna, Tenerife, Spain

11 Spanish Virtual Observatory, Spain

12 Centro Astronómico Hispano Alemán, Observatorio de Calar Alto, Sierra de los Filabres, 04550 Gérgal, Spain

13 Thüringer Landesssternwarte Tautenburg, Sternwarte 5, 07778 Tautenburg, Germany

14 Max-Planck-Institut für Astronomie, Königstuhl 17, 69117 Heidelberg, Germany

15 Departamento de Física de la Tierra y Astrofísica and IPARCOS-UCM (Instituto de Física de Partículas y del Cosmos de la UCM), Facultad de Ciencias Físicas, Universidad Complutense de Madrid, 28040 Madrid, Spain

Appendix A: Long tables

Table A.1. Date of observation, radial velocities, and chromatic index (with their associated errors) of the YZ CMi CARMENES spectroscopic observations.

HJD − 2450000 [d]	RV [m s^{-1}]	CRX [m s^{-1} Np^{-1}]
7655.71	163.5 ± 4.6	−179 ± 41
7673.66	157.8 ± 2.8	−27 ± 29
7689.73	36.6 ± 8.7	448 ± 51
7692.72	77.2 ± 5.3	234 ± 41
7699.65	275.4 ± 7.6	−369 ± 54
7704.60	231.2 ± 3.9	−164 ± 32
7735.61	310.0 ± 8.1	−411 ± 53
7755.69	158.6 ± 3.8	−119 ± 37
7756.56	59.9 ± 6.6	327 ± 45
7760.50	301.9 ± 7.6	−384 ± 51
7761.41	89.9 ± 4.1	172 ± 35
7762.62	201.9 ± 2.8	−80 ± 26
7763.53	284.4 ± 7.9	−412 ± 49
7779.46	216.7 ± 3.7	−156 ± 30
7786.49	58.7 ± 6.1	276 ± 45
7788.48	314.0 ± 9.1	−472 ± 54
7790.49	203.2 ± 4.1	−65 ± 41
7798.48	134.2 ± 3.3	138 ± 26
7800.41	49.4 ± 7.7	392 ± 45
7815.36	193.0 ± 1.6	−27 ± 16
7822.36	151.6 ± 2.9	−74 ± 26
7830.42	229.2 ± 7.4	−393 ± 44
7849.36	294.8 ± 8.6	−441 ± 56
7852.42	274.3 ± 7.7	−380 ± 57
7856.34	11.7 ± 8.4	416 ± 50
7863.38	303.4 ± 8.9	−441 ± 60
7875.36	36.7 ± 7.1	371 ± 44

Table A.2. Date of observation and normalised flux (with associated errors) of the YZ CMi TJO photometric observations.

HJD − 2450000 [d]	Norm. flux
7688.643	0.9808 ± 0.0005
7689.639	0.9827 ± 0.0005
7692.617	1.0003 ± 0.0006
7693.567	1.0348 ± 0.0005
7693.651	1.0383 ± 0.0005
7694.569	0.9655 ± 0.0007
7694.654	0.9539 ± 0.0005
7695.572	1.0207 ± 0.0009
7695.573	1.0224 ± 0.0011
7696.561	1.0122 ± 0.0006
7696.646	0.9997 ± 0.0006
7699.646	0.9854 ± 0.0005
7700.567	0.9615 ± 0.0005
7702.543	0.9833 ± 0.0005
7708.527	0.9572 ± 0.0007
7708.609	0.9489 ± 0.0004
7723.526	1.0393 ± 0.0005
7723.624	1.0371 ± 0.0005
7724.593	0.9967 ± 0.0011
7724.594	0.9930 ± 0.0005
7725.570	0.9730 ± 0.0010
7729.620	1.0390 ± 0.0012
7730.468	0.9833 ± 0.0006
7730.469	0.9769 ± 0.0012
7731.467	1.0149 ± 0.0006
7734.495	1.0202 ± 0.0007
7734.562	1.0188 ± 0.0007
7734.577	1.0327 ± 0.0008
7735.456	1.0169 ± 0.0008
7736.536	0.9608 ± 0.0009
7741.445	0.9859 ± 0.0005
7741.536	0.9658 ± 0.0005
7742.454	0.9954 ± 0.0005
7742.540	0.9913 ± 0.0005
7746.518	1.0185 ± 0.0005
7746.618	1.0133 ± 0.0007
7748.474	1.0318 ± 0.0005
7749.447	1.0068 ± 0.0006
7749.448	1.0096 ± 0.0013
7750.533	0.9696 ± 0.0005
7751.530	1.0450 ± 0.0006
7751.531	1.0458 ± 0.0011
7752.509	0.9830 ± 0.0006
7752.510	0.9827 ± 0.0007
7752.606	0.9746 ± 0.0005
7753.471	0.9873 ± 0.0008
7756.641	1.0318 ± 0.0005
7758.461	0.9522 ± 0.0004
7758.580	0.9557 ± 0.0006
7759.423	1.0204 ± 0.0005
7759.508	1.0228 ± 0.0005
7759.514	1.0246 ± 0.0005
7760.396	1.0224 ± 0.0005
7760.433	1.0126 ± 0.0005

Table A.2. continued.

HJD – 2450000 [d]	Norm. flux
7760.523	1.0015 ± 0.0009
7761.394	0.9641 ± 0.0005
7761.433	0.9624 ± 0.0011
7762.382	1.0414 ± 0.0006
7762.576	1.0411 ± 0.0005
7763.386	0.9999 ± 0.0023
7764.463	0.9722 ± 0.0006
7768.459	1.0368 ± 0.0006
7768.518	1.0264 ± 0.0006
7768.544	1.0301 ± 0.0006
7795.429	1.0149 ± 0.0015
7804.485	1.0538 ± 0.0005
7805.487	0.9620 ± 0.0005
7807.390	1.0214 ± 0.0006
7807.523	1.0124 ± 0.0007
7809.450	1.0215 ± 0.0005
7809.541	1.0282 ± 0.0006
7811.510	0.9641 ± 0.0012
7813.405	0.9986 ± 0.0006
7813.406	0.9975 ± 0.0008
7819.468	0.9528 ± 0.0009
7819.469	0.9525 ± 0.0007
7821.367	1.0319 ± 0.0018
7821.472	1.0143 ± 0.0022
7822.389	0.9565 ± 0.0007
7822.474	0.9583 ± 0.0010
7827.405	0.9807 ± 0.0010
7827.406	0.9829 ± 0.0008
7830.419	0.9633 ± 0.0011
7830.495	0.9717 ± 0.0006
7831.419	1.0008 ± 0.0007
7834.442	1.0279 ± 0.0011
7836.439	0.9720 ± 0.0005
7843.422	1.0434 ± 0.0010
7857.405	1.0412 ± 0.0006